An integrated endotracheal brachytherapy system: engineering validation and dosimetric advantages

Jerome Jean-Joseph, Christoph Westerhausen, Florian Gerheuser, Tilman Janzen, Georg Stueben, Maria Neu, Nikolaos Balagiannis

Angaben zur Veröffentlichung / Publication details:

Jean-Joseph, Jerome, Christoph Westerhausen, Florian Gerheuser, Tilman Janzen, Georg Stueben, Maria Neu, and Nikolaos Balagiannis. 2026. "An integrated endotracheal brachytherapy system: engineering validation and dosimetric advantages." *Brachytherapy* 25 (3): 455–64. https://doi.org/10.1016/j.brachy.2025.10.003.

ELSEVIER

CrossMark

BRACHYTHERAPY

Brachytherapy 25 (2026) 455–464

Original Article

An integrated endotracheal brachytherapy system: Engineering validation and dosimetric advantages

Jerome Jean-Joseph[1,*], Christoph Westerhausen[2], Florian Gerheuser[3], Tilman Janzen[1], Georg Stueben[4,5,6,7], Maria Neu[4,5,6,7], Nikolaos Balagiannis[4,5,6,7]

[1] *Medical Physics Department, Augsburg University Hospital, Augsburg, Germany*
[2] *Physiology, Institute of Theoretical Medicine, University of Augsburg, Augsburg, Germany*
[3] *Department of Anesthesiology and Surgical Intensive Care Medicine, Augsburg University Hospital, Augsburg, Germany*
[4] *Radiotherapy Department, Faculty of Medicine, University of Augsburg, Augsburg, Germany*
[5] *Comprehensive Cancer Center Augsburg (CCCA), Faculty of Medicine, University of Augsburg, Augsburg, Germany*
[6] *Comprehensive Cancer Center Alliance WERA (CCC WERA), Augsburg, Germany*
[7] *Bavarian Cancer Research Center (BZKF), Augsburg, Germany*

ABSTRACT

PURPOSE: Conventional bronchial and esophageal applicators, such as the Bonvoisin–Gérard applicator (BGA), are not optimal for tracheal brachytherapy due to uncontrolled positioning. We developed the multichannel tracheal applicator (MTA), a single-use, patient-adapted device designed for integration within standard endotracheal tubes (ETT), offering gravity-independent geometry, customizable dose delivery, and validated ventilation compatibility. The intended clinical applications include recurrent granulation tissue at stent margins and primary tracheal carcinomas.

METHODS AND MATERIALS: The study comprised three components: (1) anatomical modeling and device design based on Computed Tomography (CT) datasets from 25 patients; (2) validation of ventilation performance and positional stability using Computer-Aided Design (CAD) computational fluid dynamics (CFD) simulations and bench experiments under controlled ventilation and vibration; and (3) dosimetric evaluation with phantom radiochromic film measurements and treatment planning comparisons between MTA and BGA.

RESULTS: Airflow resistance modeling of MTA within the endotracheal tubes (ETT) showed close agreement with experimental data, with peak inspiratory pressure (PIP) differences <2% and values remaining within clinical safety limits up to 500 mL TV. Simulated motion testing confirmed positional stability (<0.5 mm displacement). Dosimetric evaluation demonstrated 99% agreement between measured and planned dose distributions. Compared to BGA, MTA demonstrated improved conformity and better sparing of organs at risk (OAR).

CONCLUSION: MTA overcomes key geometric and stability limitations of conventional applicators by enabling precise, customizable dose delivery in the trachea while preserving physiological ventilation under standard conditions. Its validated airflow resistance, positional stability, and dosimetric superiority establish strong proof-of-concept evidence. The validated engineering performance and superior dosimetric characteristics justify progression to early-phase clinical trials to evaluate safety, feasibility, and therapeutic efficacy compared to conventional approaches.

Keywords: Tracheal brachytherapy; 3D-printed applicator; Dose customization; Ventilation safety

Purpose

Recurrent granulation tissue at tracheal stent margins (Fig. 1A) causes airway obstruction in 7.9% of patients with malignant central airway obstruction (1), often requiring interventions like laser ablation, cryotherapy, or dilation, increasing morbidity (2). Early-stage tracheal carcinomas (T0–T1), such as squamous cell or adenoid cystic

Received 7 August 2025; received in revised form 2 October 2025; accepted 4 October 2025

Disclosures: The authors report no proprietary or commercial interest in any product mentioned or concept discussed in this article.

* Corresponding author. Medical Physics Department, Augsburg university hospital, Stenglinstraße 2, D-86156 Augsburg, Germany.

E-mail address: Jerome.jean-joseph@uk-augsburg.de (J. Jean-Joseph).

1538-4721/$ - see front matter
https://doi.org/10.1016/j.brachy.2025.10.003

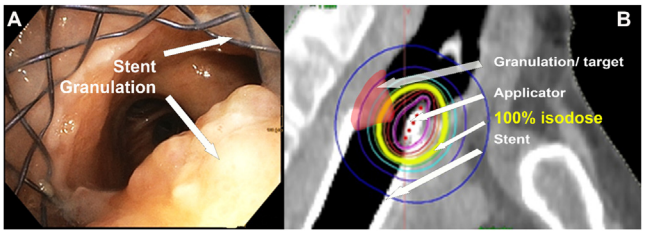

Fig. 1. Clinical rationale and limitations of single-channel tracheal brachytherapy. (A) Bronchoscopic view of granulation tissue at tracheal stent. (B) Sagittal CT demonstrating dosimetric limitations of single-channel design: the 100% isodose line (yellow) fails to encompass the complete target volume (red), with particular underdosage in superior and lateral regions, while simultaneously overdosing posterior tracheal wall and adjacent OAR.

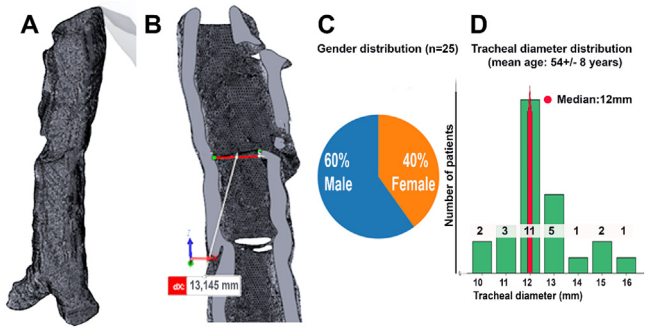

Fig. 2. Anatomical assessment guiding ETT selection (A, B): 3D tracheal reconstructions—full (A) and cross-sectional (B) views; (C): gender distribution; (D): distribution of minimum tracheal diameters.

carcinoma, are rare, aggressive tumors in the proximal trachea (3). Per the AJCC 8th edition (4), T0 indicates carcinoma in situ, and T1 denotes tumors ≤2 cm confined to the tracheal mucosa or submucosa, making them ideal for high-dose-rate (HDR) brachytherapy.

HDR brachytherapy shows promise for tracheal malignancies and granulation tissue (5,6), but conventional endobronchial applicators are suboptimal for tracheal granulation or asymmetric carcinomas.

The single-channel applicator developed by Fritz et al. (5) represents a significant advancement over earlier designs by incorporating a centering mechanism to position the radioactive source at the geometric center of the bronchial lumen, thereby reducing the dose heterogeneity observed with noncentered catheters. As detailed in the GEC-ESTRO handbook (6), this approach effectively addresses symmetric bronchial lesions by ensuring uniform radial dose distribution. However, this single-channel design has inherent limitations when applied to tracheal pathologies, particularly asymmetric lesions or granulation tissue with irregular morphology. The fixed single-source geometry often results in overdosing of the posterior tracheal wall while underdosing superior and lateral regions (Fig. 1B), increasing toxicity risks to normal tissues while potentially compromising tumor control.

The tracheal wall, with 1.2 mm thick cartilage rings and membranous intervals, presents geometric challenges for dose delivery, requiring precise targeting to avoid stenosis or fistula. Balloon-based applicators, used in esophageal brachytherapy, are contraindicated in the trachea due to airway obstruction risks, especially in ventilated patients. Innovative applicator designs are needed to ensure airway patency and dose conformity for both symmetric and asymmetric tracheal lesions.

Methods and materials

This study comprised three integrated components: (1) anatomical modeling and device design optimization based on clinical CT datasets from 25 patients; (2) computational and experimental validation of ventilation performance and mechanical stability under physiological conditions and (3) dosimetric evaluation using phantom-based measurements and comparative treatment planning analysis.

For dosimetric evaluation, target volumes were defined based on clinical data from our cohort, where granulation tissue represented the predominant indication (85% of cases) compared to early-stage tracheal carcinomas (T0-T1). Quantitative analysis revealed granulation lesions with mean longitudinal extent of 1.9 ± 0.4 cm and protrusion depth of 0.45 ± 0.15 cm, yielding average dimensions of 2.0 cm length, 0.5 cm thickness, and 2.0 cm^3 volume. These metrics, derived from the 21 granulation cases in our cohort, established the phantom geometry for comprehensive dose validation studies.

1 Patient population analysis

We conducted a retrospective review of 25 patients with tracheal stenosis, processing CT datasets using 3D Slicer (version 4.11, The Surgical Planning Laboratory, USA) (7) to generate anatomical reconstructions (Fig. 2A–B). The cohort (mean age 54 ± 8 years) demonstrated a median narrowest tracheal diameter of 12.0 mm (IQR: 11.0–13.0 mm), with 20% exhibiting diameters ≤11.0 mm. Based on these measurements (Fig. 2D), we conservatively selected a 10.6 mm outer diameter (OD) endotracheal tubes (ETT) 8 mm inner diameter (ID) to ensure compatibility with narrow anatomical variants while maintaining adequate ventilation.

These anatomical measurements also informed our organs at risk (OAR) characterization, with cartilage thickness averaging 1.2 mm (range: 1.0–1.5 mm) across the 25 patient datasets.

System components

MTA, a three-component applicator, is engineered to prevent disassembly or lung migration during use and is adapted for magnetic resonance imaging (MRI) and CT imaging.

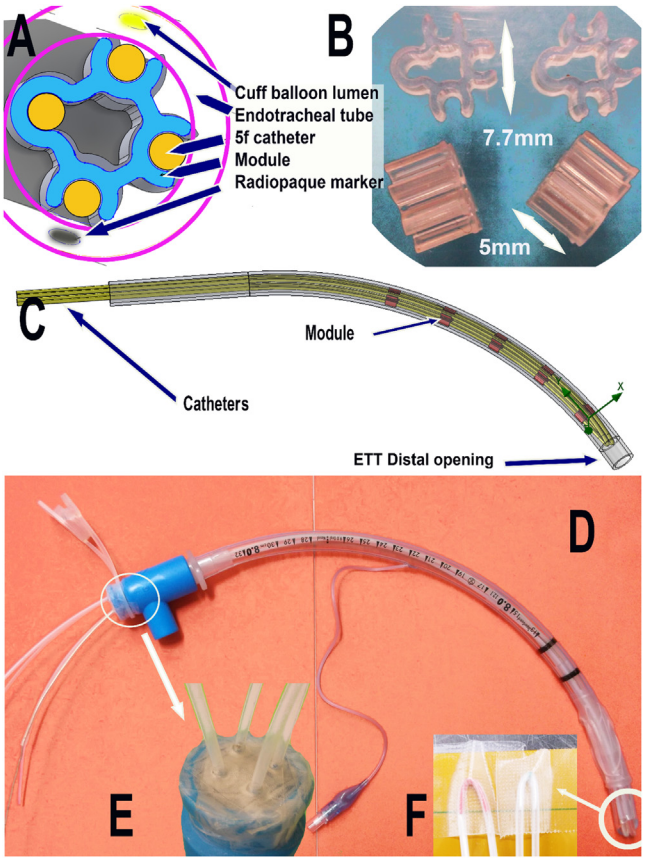

Fig. 3. MTA assembly with modular components. (A) Cross-section highlighting key elements; (B) 3D-printed modules; (C) CAD model of MTA; (D) MTA; (E) Overview showing antileakage integration, (F) Folded 2-meter catheter yields 1-meter dual-channel configuration with radiopaque and MR-visible tip.

ETT

A polyvinyl chloride (PVC) medical-grade ETT (Shiley, Covidien, USA) (Fig. 3D) was conservatively sized to balance applicator accommodation with patient safety. An OD of 10.6 mm (ID: 8.0 mm) was selected based on compatibility with adult tracheal anatomy (8) while minimizing tracheal trauma risk (9). Larger tubes (outer diameter >12 mm) increase complication risks, including excessive tracheal wall pressure and mucosal injury from cuff overinflation (10).

The selected ETT diameter, positioned below the cohort median tracheal diameter of 12.0 mm (Fig. 2C), enables controlled in situ rotation (0–45°) to facilitate flexible catheter arrangements in either square or diamond configurations (Fig. 8D–E). The tube interface maintains full compatibility with standard anesthesia equipment while securely housing the embedded catheter modules. An airtight seal preventing air leakage is achieved using a polyacrylate adhesive fixation bandage (Leukoflex, Essity, Sweden; Fig. 3E).

Folded catheter array

The radiation delivery system uses two 2-meter-long, 5F nylon 6/6 tubes (1.67 mm OD; Zeus Industrial Products, USA). Each tube is folded in half to form a 1-meter dual-channel catheter (Fig. 3F), resulting in four separate pathways for precise positioning of the iridium-192 source. This design allows flexible source placement while ensuring structural stability. Each catheter includes a 5 mm Titanium guidewire tip to enhance visualization during CT or MRI imaging (Fig. 3F).

3D-Printed centering modules

Five centering modules (Fig. 3A–B) were designed using CAD software (SOLIDWORKS 2023 SP5 Premium, Dassault Systèmes, USA) and manufactured from USP Class VI certified BioMed Amber biocompatible photopolymer resin (Formlabs, Massachusetts, USA) (11) via stereolithography (SLA). The modules ensure submillimeter positioning accuracy of four radiation channels within the ETT lumen, maintaining mechanical stability during clinical handling and preventing catheter displacement throughout therapy delivery. The five-module configuration, spaced at 2.5 cm intervals, represents the optimal balance between catheter parallelism and airflow dynamics as determined through computational optimization.

2 Ventilation compatibility: computational and experimental testing

To evaluate airflow resistance, both computational fluid dynamics (CFD) simulations and bench experiments were performed.

1. Experimental setup**:** Ventilation tests used a Dräger Atlan A350 ventilator connected to a tracheal phantom and calibrated 1 L test lung (Siemens, Germany). TV of 400–550 mL were delivered at 13 breaths/min with 5 cmH_2O positive end-expiratory pressure. PIP were recorded under baseline conditions (ETT only) and with MTA integrated.
2. CFD modeling**:** The CAD model of MTA was meshed (2.8 million elements) and imported into COMSOL Multiphysics (v6.2, COMSOL AB, Sweden). The realizable k–ε turbulence model was applied, solving continuity and Navier–Stokes momentum equations, as well as transport equations for turbulent kinetic energy and dissipation rate. Boundary conditions replicated experimental TV and pressures. Agreement within 5% between simulation and bench measurements was considered validation.

CFD validation protocol

To isolate MTA-specific impact on airflow resistance while reducing computational complexity (12), a bound-

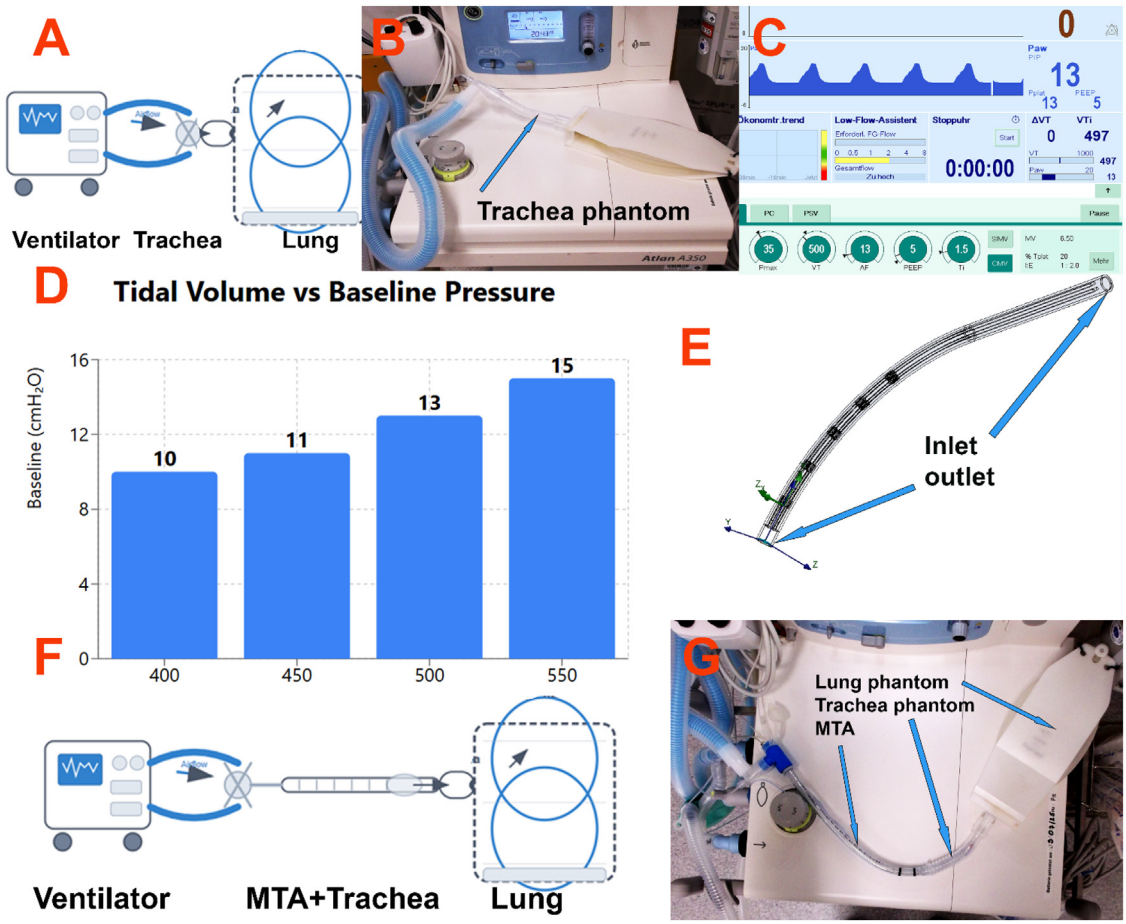

Fig. 4. MTA ventilation validation protocol. (A–B): Setup without MTA, (C): Ventilator results without MTA at TV: 497 ml, (D): Baseline PIP without MTA, (E): CFD MTA boundaries, (F–G): Setup with MTA.

ary condition calibration strategy was employed. Experimental PIP values were initially obtained under baseline conditions—i.e., with the ventilator circuit operating without MTA—to establish reference parameters (Fig. 4A). Measurements were performed using an Atlan A350 ventilator (Dräger, Germany) connected to a tracheal phantom and a calibrated 1 L test lung (Siemens, Germany), designed to replicate physiological respiratory mechanics (Fig. 4B). TV of 400, 450, 500, and 550 mL were applied at a constant respiratory rate of 13 breaths per minute and positive end-expiratory pressure (PEEP) of 5 cmH_2O (Fig. 4C). Baseline PIP values ranged from 10 to 13 ± 0.5 cmH_2O (Fig. 4D), depending on TV, and were used as physiological outlet boundary conditions in CFD simulations of MTA-only geometry (Fig. 4E).

In the simulations, inlet volume flow rates were prescribed to reproduce the experimental TV profiles accurately, ensuring that time-averaged flows matched volume delivery. The outlet pressure was fixed at the experimentally determined baseline PIP values (Fig. 4D), representing downstream resistance without MTA. The purpose of this calibration was to ensure that any additional pressure drop observed in simulation could be attributed solely to MTA contribution.

Based on the successful validation of our setup for the standalone ETT (simulated vs. experimental agreement; Fig. 6C), we extended its use to assess MTA.

Experimental setup

To validate model fidelity, simulated PIP values at MTA inlet were directly compared with ventilator-derived PIP measurements obtained from the physical setup with MTA integrated (Fig. 4F). The CFD model would be considered validated for clinical application if experimental measurements demonstrated quantitative agreement with simulations (error threshold: $\leq 5\%$). Should this criterion be satisfied, the model would subsequently be employed to predict airflows for specific MTA configurations.

All experiments maintained standardized conditions (T°:22°C, P°: 1atm) to ensure reproducibility. It was verified that no leakage was present in MTA ($\Delta TV = 0$, Figs. 3E and 4C).

CFD methodology

Geometry and meshing

MTA CAD model (Fig. 4E) was exported as a watertight STereoLithography (STL) mesh with a surface deviation tolerance of 0.1 mm, then imported into COMSOL Multiphysics (v6.2.0.423, COMSOL AB, Sweden). Automated mesh validation confirmed geometric discrepancies of less than 0.05 mm relative to the native CAD geometry.

The computational domain was discretized using a tetrahedral mesh incorporating prismatic near-wall layers to accurately resolve boundary gradients. Grid independence was established through Richardson extrapolation analysis (13), yielding a final mesh comprising 2.8 million elements.

Flow modeling

- Given the turbulent flow regime in the ETT (Re = 3690; ID = 8.0 mm (14)), a turbulence model validated for ETT-scale applications was essential. The realizable k–ε model with standard wall functions met this criterion, demonstrating <4.8% error in velocity profiles at comparable Re (3500–4000) (15). These equations were numerically solved using COMSOL Multiphysics, which implemented the finite element method to discretize and solve the governing equations. The software automatically handled the numerical solution process, including mesh generation, boundary condition application, and convergence criteria. The COMSOL software automatically discretized and solved the following governing equations using the finite element method:
- Continuity: $\nabla \cdot u = 0$
- Momentum (Navier-Stokes):

$$\rho(u \cdot \nabla)u = -\nabla p + \mu\nabla^2 u + \nabla \cdot \tau_t$$

- Turbulent kinetic energy (k):

$$\rho\partial_t(uk) + \rho u_j \partial_j k = \tau_{ij}\partial_j u_i - \rho\varepsilon + \nabla \cdot [(\mu + \mu_t/\sigma_k)\nabla k]$$

- Turbulence dissipation rate (ε):

$$\rho\partial_t(u\varepsilon) + \rho u_j \partial_j \varepsilon = C_1\varepsilon\tau_{ij}\partial_j u_i - C_2\rho k\varepsilon^2 + \nabla \cdot [(\mu + \mu_t/\sigma\varepsilon)]\nabla\varepsilon$$

Boundary conditions and analysis

The computational model employed (Fig. 4E) physiologically representative boundary conditions: At the inlet, we applied a volume flow rate waveform calibrated to match experimentally measured TV (16). The outlet boundary (Fig. 4E) was prescribed as a fixed pressure condition set to baseline PIP values derived from clinical data (Fig. 4D). All wall surfaces enforced a no-slip boundary condition with zero velocity relative to stationary anatomy.

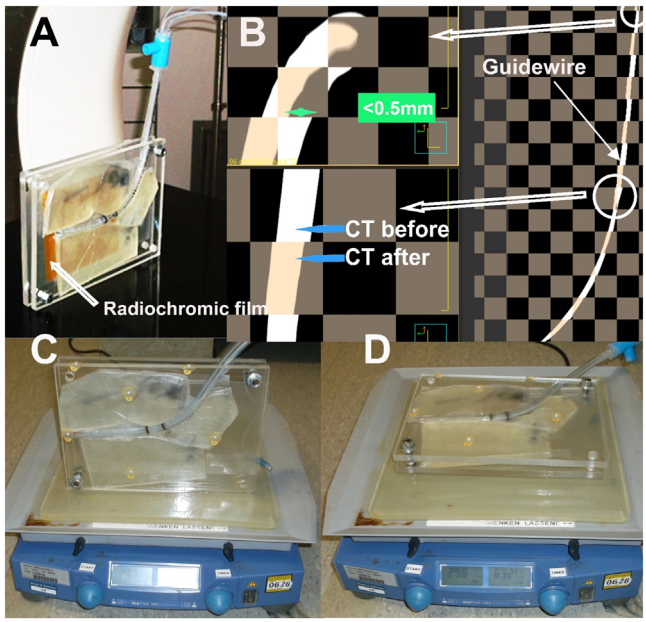

Fig. 5. Phantom setup and vibration test validation. (A): phantom integrated with radiochromic film (orange layer) for dosimetric evaluation. (B): CT image overlay demonstrating sub-millimeter catheter stability postvibration testing. (C): Phantom mounted on a linear shaker in longitudinal orientation (simulating supine patient positioning. (D): Phantom reconfigured in transverse orientation on the shaker (simulating lateral patient positioning).

3 Phantom Design and Fabrication

A phantom model was constructed to replicate human airway anatomy from the oropharynx to the carina. The phantom comprised two optically transparent plexiglas plates ($25 \times 15 \times 1$ cm^3) sandwiching a 1-cm-thick layer of tissue-equivalent bolus material (ExaFlex Bolus, Medisynt, Germany) to simulate soft-tissue friction and mechanical properties. This design enabled:

Real-time visualization of ETT placement through transparent walls,

Precise geometric referencing via embedded fiducial markers for reproducible component alignment, Modular interchangeability of anatomical segments to facilitate repeated ETT insertion and catheter positioning.

The phantom supported controlled experimental validation of:

Dose distribution via radiochromic film (EBT3, Gafchromic, Ashland Inc., Wayne, NJ, USA) placement at predefined anatomical landmarks,

Catheter stability metrics through sequential repositioning trials (Fig. 5C–D).

Mechanical stability assessment

Per ISO 13485:2016 (Clause 7.3.3.2) (17), MTA's single-use designation inherently eliminates cyclic fatigue hazards, rendering fatigue testing inapplicable under ISO 14971:2019′s risk-based framework (Clause 6.3) (18). Mechanical stability was therefore validated against worst-case single-insertion scenarios using an IKA HS 260 control shaker (IKA-Werke, Germany), with vibration parameters (5 Hz frequency, 2.0 cm amplitude) selected from published biomechanical data representing spontaneous respiratory motion and head/neck displacements during ventilation and manipulation (19). The protocol ($n = 3$) comprised two sequential 30-minute phases: longitudinal vibration (Fig. 5C) (simulating supine positioning) and transverse vibration (Fig. 5D) (simulating positional changes), during which ETT lumen physically constrained radial displacement (≤0.5 mm) while permitting clinically relevant longitudinal movement. Quantitative assessment via pre and post-test CT scans (Siemens Somatom; 0.5×0.5 mm in-plane resolution and 1.0 mm slice thickness) with laser-guided phantom alignment confirmed maximum displacement of 0.5 mm—measured using Pinnacle³ treatment planning software (v16.2, Philips, Netherlands) (Fig. 5B) on catheter guidewire positions. Environmental conditions ($22.0°C \pm 1.0°C$, 1 atm) were maintained throughout testing.

For a complete visual demonstration of the assessment methodology, including equipment setup and measurement techniques, refer to Video 1 in the supplementary materials.

Irradiation setup

To optimize the applicator's performance, we conducted initial validation using radiochromic film (20). This step was crucial in determining the precise offset (−7 mm) and appropriate indexer length (+990 mm) for our HDR afterloader (MicroSelectron, Elekta AB, Sweden), which utilized an iridium-192 (Ir-192) source with an air kerma strength of 41.07 $\mu Gy \cdot m^2 \cdot h^{-1}$ (source dimensions: 3.5 mm length × 0.6 mm diameter).

Dosimetric comparison methods

For dosimetric validation, a total of 3 radiochromic films (EBT3, Gafchromic, Ashland Inc., Wayne, NJ, USA) were irradiated at predefined anatomical landmarks within the phantom. The films were scanned using an Epson Perfection V750 Pro scanner (Seiko Epson Corporation, Suwa, Japan) at 96 dpi resolution and 48-bit color depth. Gamma analysis was performed with the VeriSoft software package (PTW, Freiburg GmbH, Germany) using stringent acceptance criteria (2 mm DTA / 2.3% dose difference). These procedures were used to compare experimental film measurements with Oncentra Brachy 4.6.2 dose calculations. A total of three radiochromic films were irradiated, of which one representative dataset was analyzed for gamma comparison (20).

Results

Ventilation performance analysis

CFD simulations demonstrated agreement within <2% of experimental measurements, validating the accuracy of pressure predictions across TV (Fig. 6C). Notably, the simulated PIP remained below 30 cmH_2O at a TV of 500 mL (27 cmH_2O) (Fig. 6C), remaining within clinically accepted safety thresholds for patient ventilation (21). These findings suggest MTA introduces moderate hemodynamic resistance (22) while maintaining flow stability within acceptable limits for clinical use.

Computational optimization identified the clinically optimal modular configuration via iterative parametric analysis of module count (3–7 segments) and inter-module spacing (2.0–3.0 cm), constrained by displacement limits (<0.5 mm) and catheter parallelism (<2° angular deviation). A configuration of five modules spaced 2.5 cm apart emerged as the Pareto-optimal solution, offering the best trade-off among competing objectives. By distributing mechanical resistance along MTA's length, it effectively reduced localized pressure peaks at the module sites. Experimental validation closely matched simulation results, with PIP deviations ≤1.7% across tested TV (400–550 mL; Fig. 6C). At 2.5 cm, intermodule spacing delivered the optimal compromise: preserved catheter parallelism and enhanced airflow dynamics (Fig. 6D), validating MTA's engineered geometry for stable ventilator compatibility. This configuration mitigates alveolar overdistension by optimizing pressure. These findings underscore MTA's potential to integrate into standard ventilation protocols without compromising patient safety or mechanical integrity (Fig. 7).

Vibration stability assessment

MTA demonstrated positional stability under simulated physiological motion, with sub-millimeter displacement observed across all test conditions. High-resolution CT analysis confirmed a mean displacement of 0.43 ± 0.14 mm relative to anatomical landmarks, consistently below the 2 mm clinical threshold requiring catheter repositioning.

No statistically significant differences emerged between patient position:

Supine-simulated positioning: 0.43 ± 0.14 mm displacement

Lateral-simulated positioning: 0.33 ± 0.15 mm displacement

The observed stability (<0.5 mm shift) remained consistent across all trials ($n = 3$), with displacement vectors confined to the longitudinal axis of the tracheal phantom. These findings confirm that MTA maintains precise

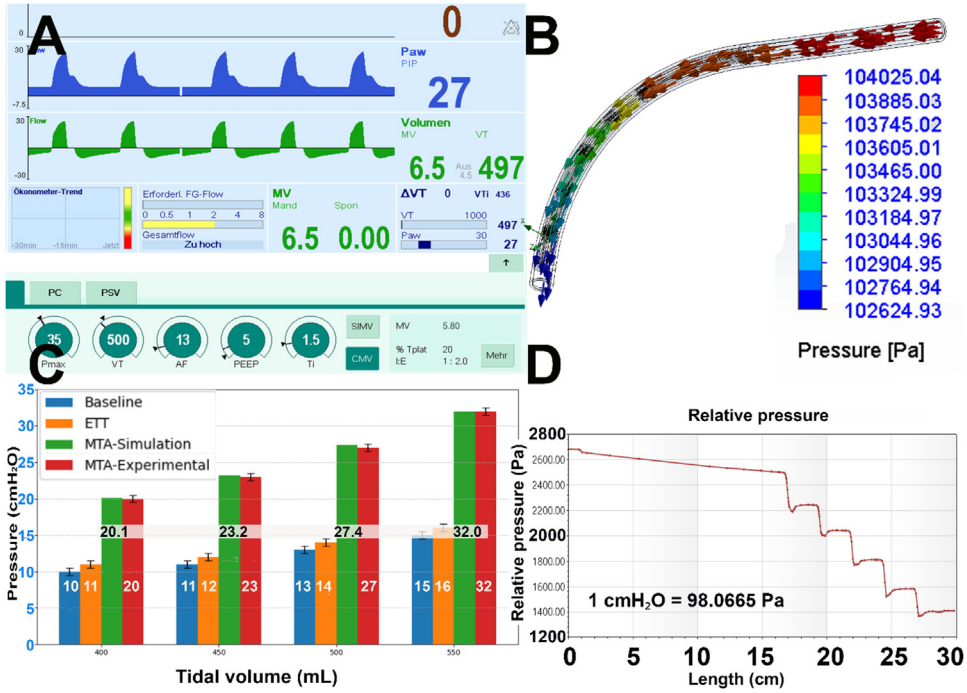

Fig. 6. MTA airflow performance validation. (A): Dräger Atlan A350 ventilator interface during MTA testing at TV= 497 mL. (B): CFD simulation of airflow trajectories within MTA at TV = 500 mL. Color gradients represent pressure distribution (Pa), with red denoting high-pressure zones at the inlet. (C): Comparative analysis of experimental vs. simulated PIP across TV (400–550 mL). Baseline measurements (blue) reflect native tracheal resistance, while ETT (orange) and MTA green/red) curves demonstrate device-specific pressure contributions. Error margins (<2%) validate CFD accuracy. (D): Relative pressure drop along MTA length at TV = 500 mL.

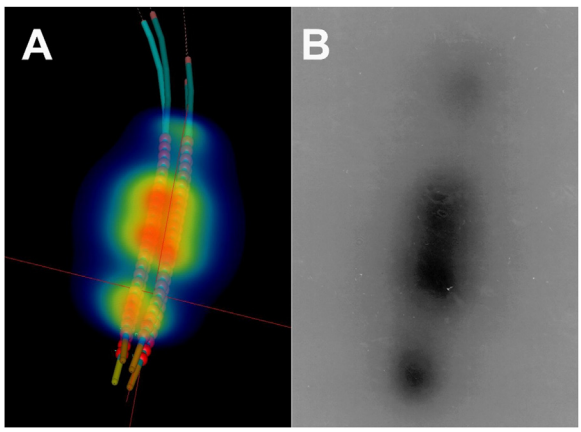

Fig. 7. Validation of MTA Dose Delivery (A): 3D isodose map generated via treatment planning software. (B): Irradiated radiochromic film. Comparison of MTA Versus BGA.

catheter positioning during clinically relevant mechanical perturbations, satisfying safety requirements without necessitating repositioning interventions.

Dosimetric validation results

The Gamma analysis demonstrated <2.3% deviation between measured and calculated dose distributions, yielding a 99.0% gamma pass rate—exceeding the 95% clinical threshold. This confirms the accuracy of the experimental setup and validates the dosimetric performance of MTA (23). This high-precision result validates both the correct offset and catheter length in the experimental setup, while confirming that phantom heterogeneities did not significantly impact dose calculation accuracy.

Comparative analysis (23) of BGA (6 mm OD, Elekta, Sweden) (Fig. 8A) versus MTA configured in square (Fig. 8D) and diamond (Fig. 8E) geometries reveals that while all three configurations achieve adequate target coverage (Fig. 8F) at the prescription dose level (D100%), the diamond configuration offers the most favorable balance between conformality and OAR sparing. Specifically, D150% and D200% volumes within the target are significantly reduced in the diamond configuration (32.0% and 7.0%, respectively) compared to BGA (50.1% and 5.2%) and square MTA (48.7% and 16.0%). OAR doses are substantially higher for BGA design (e.g., D100% = 33.7%) versus near-complete OAR sparing in both MTA configurations (D100% = 2.3% and 0.0% for square and diamond, respectively). The Conformity Index (COIN) is highest for the diamond configuration (0.73), while the Dose Non-Uniformity Ratio (DNR) is lowest (0.42), indicating more precise dose shaping and better homogeneity.

The diamond configuration yields significantly improved OAR sparing and lower high-dose exposure within the target compared to BGA approach (Fig. 8C).

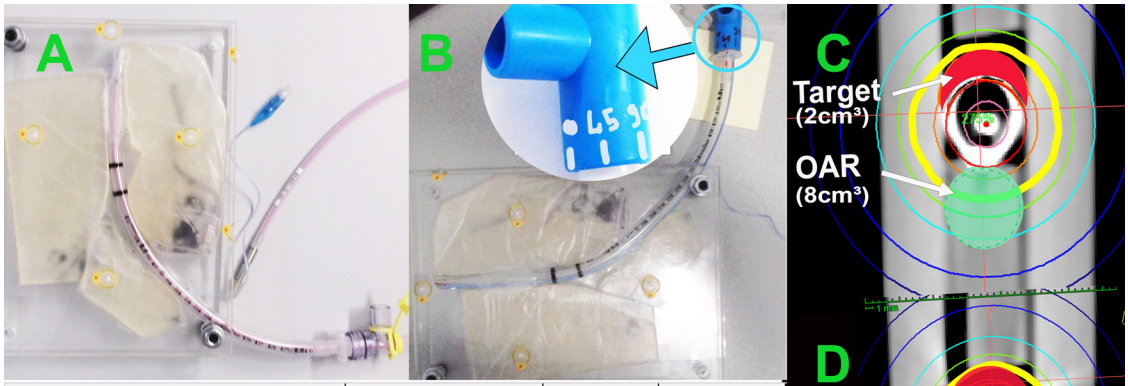

F	Single channel	Square	Diamond
V100%Target (Volume in cm³)	100 (2)	99,9(2)	100(2)
V150%Target (Volume in cm³)	50,1(1)	48,7(.97)	32(.64)
V200%Target (Volume in cm³)	5,2(.1)	16(.32)	7(.14)
V100%OAR (Volume in cm³)	33,7(2.7)	2,3(.18)	0(0)
V150%OAR (Volume in cm³)	11,4(.91)	0(0)	0(0)
V200%OAR (Volume in cm³)	1,5(.12)	0(0)	0(0)
DNR	0,52	0,51	0,42
COIN	0,45	0,61	0,73

Fig. 8. Experimental comparison of BGA and MTA. (A): BGA inserted into a phantom.
(B): MTA positioned in the phantom; the inset shows the proximal connector with angle. (C): Isodose distribution for BGA configuration. D: Isodose distribution for MTA in square geometry (0°). E: Isodose distribution for MTA in diamond geometry (45°). F: Quantitative comparison of dosimetric indices across all three configurations. Green values indicate the most favorable (optimal) results for each index, while red highlights the least favorable (suboptimal) values.

Discussion

The development of MTA addresses critical gaps in tracheal brachytherapy, driven by the unavailability of the Fritz applicator in Elekta's European catalog. MTA demonstrated markedly superior dosimetric performance compared to BGA, which is often adapted for airway brachytherapy. In the diamond configuration, MTA achieved effective sparing of OAR, with D100% values of 0.0% versus 33.7% for BGA, while maintaining superior dose conformity (COIN = 0.73 vs 0.51). These dosimetric improvements translate to substantial clinical benefits. Conventional single-channel applicators often necessitate dose de-escalation to limit OAR toxicity, potentially compromising local control rates. The enhanced conformity achieved with MTA enables dose escalation to biologically effective levels while maintaining safety margins for critical structures. This capability is particularly relevant for adenoid cystic carcinomas, which require high doses due to their radioresistant nature, and for granulation tissue control, where inadequate dosing leads to treatment failure and repeated interventions.

OAR were comprehensively defined as tracheal cartilage (mean 1.2 mm thickness, range 1.0–1.5 mm), esophageal wall (3.5 mm at the tracheoesophageal interface), and mediastinal structures 5–10 mm beyond the adventitia (24). Conservative dose constraints applied to tissue beyond 3 mm from the target minimize risks of radiation-induced stenosis, ulceration, and tracheoesophageal fistula. While this study employed TG-43 formalism with excellent validation results (99% gamma pass rate), model-based dose calculation algorithms (MBDCA) could improve dose accuracy by approximately 5–8% at air–tissue interfaces prevalent in tracheal anatomy (23). However, phantom validation suggests minimal clinical impact of heterogeneity corrections in our specific application, as tissue-equivalent bolus closely approximates tracheal wall properties. Clinical implementation should incorporate MBDCA for patients with anatomical variations or metallic stents where tissue heterogeneities would be more pronounced.

MTA development integrated computational fluid dynamics (CFD) with experimental validation, achieving <2% error between simulated and measured ventilation

parameters across 400–550 mL TV (20). This CAD–CFD–prototype workflow reduced trial-and-error prototyping, accelerated design optimization, and enabled patient-specific customization, aligning with EU MDR 2017/745 regulations (25).

The modular design adapts to anatomical variations, including narrower tracheal diameters in female patients or stenotic cases. This computational framework enables machine learning integration for optimized, patient-specific designs, consistent with the EU Artificial Intelligence Act (26). Similar principles could extend to other intraluminal sites requiring conformal brachytherapy delivery.

Current prototypes employ USP Class VI nonbiodegradable polymers ensuring robustness and preventing particle migration. As single-use devices subject to the EU single-use plastics directive (27), future iterations should explore bioresorbable materials like polydioxanone or PGLA, maintaining structural integrity during treatment while meeting respiratory stress requirements.

MTA's composition suggests MRI compatibility, potentially facilitating integration into MRI-based workflows. Enhanced soft-tissue delineation could improve target definition and enable dose escalation while maintaining OAR safety.

MTA addresses longstanding limitations in tracheal brachytherapy by combining precise geometry control, validated ventilation safety, and adaptable design principles. With demonstrated OAR sparing improvements and superior dose conformity, MTA establishes a platform for personalized airway brachytherapy. Early-phase clinical studies are warranted to validate safety and assess therapeutic outcomes.

Conclusion

MTA represents a novel approach to tracheal brachytherapy that demonstrates preliminary technical feasibility through CFD analysis, dosimetric validation, and phantom evaluation (28). This proof-of-concept study establishes the foundational engineering and dosimetric characteristics of MTA design. The 3D-printable, ETT-specific design concept aligns with emerging trends in personalized medical device manufacturing.

These results justify immediate progression to prospective cohort validation, positioning MTA as a technically mature solution ready for clinical translation.

Acknowledgments

The authors acknowledge Jon Yates (3d Nation GmbH) for assistance with 3D printing, Dr. Antonio Carvalho and Prof. Alexandra Jördening for insightful suggestions and Manuel Hoffman (Zeus Industrial Products Ltd.) for fruitful discussions regarding nylon tubes. We also thank Bettina Gleissner for her critical assistance in translating and editing this manuscript.

Supplementary materials

Supplementary material associated with this article can be found, in the online version, at doi:10.1016/j.brachy.2025.10.003.

References

[1] Sabath B, Casal R. Airway stenting for central airway obstruction: a review. *Mediastinum* 2023;7:18. doi:10.21037/med-22-65.
[2] Ost DE, Shah AM, Lei X, et al. Respiratory infections increase the risk of granulation tissue formation following airway stenting in patients with malignant airway obstruction. *Chest* 2012;141(6):1473–1481. doi:10.1378/chest.11-2005.
[3] Choudhury BK, Barman G, Singh S, Ahmed K. Adenoid cystic carcinoma of the upper trachea: a rare neoplasm. *J Clin Imaging Sci* 2013;3:39. doi:10.4103/2156-7514.119021.
[4] Amin MB, Edge SB, Greene FL, et al. AJCC cancer staging manual. Springer International Publishing, New York, 2017.
[5] Fritz, P. et al. A new applicator, positionable to the center of tracheobronchial lumen for HDR-IR-192-afterloading of tracheobronchial tumors International Journal of Radiation Oncology, Biology, Physics, Vol. 20, no. 5, 1061–1066
[6] Gerbaulet A, Pötter R, Mazeron JJ, et al. GEC-ESTRO bronchus cancer. Handbook of brachytherapy. Brussels: ESTRO; 2017. p. 731–46. Available from: https://user-swndwmf.cld.bz/27-Bronchus-Cancer/4.
[7] Shiaa W, Abdulghafour A, Hassoon O. 3D reconstruction from CT images utilizing the open-source tool. *AIP Conf Proc* 2024;3094:060024. doi:10.1063/5.0202322.
[8] Mir F, Sandhu G, Poncia J. Size matters: choosing the right tracheal tube. *Anaesthesia* 2012;67:1402–1403. doi:10.1111/anae.12026.
[9] Passera E, Orlandi R, Calderoni M, et al. Post-intubation iatrogenic tracheobronchial injuries: the state of art. *Front Surg* 2023;10:1125997. doi:10.3389/fsurg.2023.1125997.
[10] Formlabs. Dental LT Clear Resin. Technical Data Sheet no. 2001403 Rev 01 [Internet]. Formlabs Somerville (MA), 2020. [cited 2024 Jan 1]. Available from https://formlabs-media.formlabs.com/datasheets/2001403-TDS-ENUS-0.pdf .
[11] Lassila T, Manzoni A, Quarteroni A, Rozza G. Model order reduction in fluid dynamics: challenges and perspectives. In: Quarteroni A, Rozza G, editors. Reduced Order Methods for Modeling and Computational Reduction. Cham: Springer; 2014. p. 235–73.
[12] Chang CL, Venkatachari B, Cheng G. Tetrahedral-mesh simulation of turbulent flows with the space-time conservative schemes. In: 22nd AIAA Computational Fluid Dynamics Conference. Dallas, TX. Reston (VA): American Institute of Aeronautics and Astronautics; 2015.
[13] Xu J, Yu H, Deng J, et al. Study of compressible flow in pipes containing mesh structures. In: Proceedings of the 31st International Conference on Nuclear Engineering. Kyoto, Japan. New York: American Society of Mechanical Engineers; 2024.
[14] Kollmann W. Navier-Stokes equations. In: Kollmann W, editor. Computational fluid dynamics. Cham: Springer; 2024. p. 15–42.
[15] Monjezi M, Rismanian M, Kiani A, et al. Evaluation of the tracheal stenosis effects on airway resistance and work of breathing using computational fluid dynamics. *Tanaffos* 2023;22(2):209–214.
[16] International Organization for Standardization. Medical devices — Quality management systems — Requirements for regulatory purposes, 13485. ISO, Geneva, 2016.
[17] International Organization for Standardization. Medical devices — Application of risk management to medical devices, 14971. ISO, Geneva, 2019.

[18] Bao YD, Qu SQ, Wei W, et al. Investigation on forced vibration characteristics of Nitinol tracheal stent. *Biomed Eng Online* 2022;21:85. doi:10.1186/s12938-022-01054-y.

[19] Kumazaki Y, Hirai R, Igari M, et al. Development of an HDR-BT QA tool for source position verification. *J Appl Clin Med Phys* 2020;21(12):84–89. doi:10.1002/acm2.13063.

[20] Jean-Joseph J, Balagiannis N, Scheppach MW, et al. Auxetic solution for enhanced esophageal brachytherapy applicator. *J Contemp Brachytherapy* 2025;17(1):33–42. doi:10.5114/jcb.2025.147780.

[21] Brower RG, Matthay MA, Morris A, et al. Ventilation with lower TV as compared with traditional TV for acute lung injury and the acute respiratory distress syndrome. *N Engl J Med* 2000;342(18):1301–1308. doi:10.1056/NEJM200005043421801.

[22] Borlino S, Hagry J, Lai C, et al. The effect of PEEP on pulmonary vascular resistance depends on lung recruitability in ARDS patients. *Am J Respir Crit Care Med* 2024;210(7):856–865. doi:10.1164/rccm.202402-0383OC.

[23] Jamema SV, Nojin Paul S, Phurailatpam R, et al. Impact of inhomogeneity corrected dose calculation of clinical brachytherapy sites. *IFMBE Proc* 2015;51:463–466. doi:10.1007/978-3-319-19387-8_113.

[24] Al Khatib S, Asha W, Khzouz O, et al. Advanced tracheal adenoid cystic carcinoma with thyroid invasion mimicking thyroid cancer treated with definitive radiation: case report and review of the literature. *Case Rep Oncol* 2017;10(2):706–712. doi:10.1159/000479225.

[25] European Parliament and Council. Regulation (EU) 2017/745 on medical devices. Off J Eur Union. 2017; L 117:1–175

[26] Off J Eur Union. European Parliament and Council; 2024. p. 1–349.

[27] European Parliament and Council. Directive (EU) 2019/904 on the reduction of the impact of certain plastic products on the environment. Off J Eur Union. 2019; L 155:1–19.

[28] Jean-Joseph J, Westerhausen C, Doescher J, et al. Development and validation of the Augsburg Nasopharyngeal applicator: enhancing efficacy in Nasal route brachytherapy. *Adv Radiat Oncol* 2025;10(11):101896. doi:10.1016/j.adro.2025.101896.